

Complex symmetry of phases and magnetic properties of EuTiO_3


P. Pappas,¹ A. Bussmann-Holder^{2,*}, H. Keller,³ E. Liarokapis¹, and K. Roleder⁴

¹Department of Physics, National Technical University of Athens, Athens 15780, Greece

²Max-Planck-Institute for Solid State Research, Heisenbergstr.1, D-70569 Stuttgart, Germany

³Physik-Institut der Universität Zürich, Winterthurerstr. 190, CH-8057 Zürich, Switzerland

⁴Institute of Physics, University of Silesia, ul. 75 Pułku Piechoty 1, 41-500 Chorzów, Poland

 (Received 30 June 2022; revised 5 October 2022; accepted 21 November 2022; published 13 December 2022)

Some puzzling and unexplained observations regarding the cubic to “tetragonal” phase transition at $T_S = 282$ K in the almost-multiferroic perovskite EuTiO_3 have been reanalyzed to obtain deeper insight into the true structure and magnetic activity evolving below T_S . For this purpose, birefringence and high-quality synchrotron x-ray-diffraction (XRD) data have been used where zero magnetic field data are compared to data under the influence of a direction-dependent magnetic field. The birefringence data have been analyzed with respect to the angle dependence of the domain orientation from which the dominance of the monoclinic symmetry is unambiguously proven. The XRD structural data have been taken as input to derive the magnetic exchange constants, the related Néel temperatures T_N , and the energies of the possible magnetic ground states. Taking both results together we conclude that below T_S the symmetry cannot be tetragonal, but only monoclinic followed by another symmetry lowering transition around $T^* \approx 210$ K. In addition, the involved magnetic exchange interactions have been calculated based on the experimental lattice constants, and it is shown that these support the conclusion that any kind of magnetism stems from a competition of the various ground-state energies and consequently induces a highly frustrated magnetically active state near room temperature.

DOI: [10.1103/PhysRevB.106.214306](https://doi.org/10.1103/PhysRevB.106.214306)

I. INTRODUCTION

EuTiO_3 (ETO) is a typical perovskite oxide and very analogous to the other titanates CaTiO_3 (CTO), BaTiO_3 (BTO), SrTiO_3 (STO), and PbTiO_3 (PTO) which are all cubic at high temperatures. Depending on the *A*-site ion, either a single structural phase transition to tetragonal or lower symmetry is observed as in STO, PTO, and ETO, or a sequence of symmetry-lowering transitions take place realized in CTO and BTO [1]. In all the above compounds a long-wavelength optic mode softening takes place which is typical for a displacive phase transition to a ferroelectric state. While this is indeed observed in BTO and PTO, ETO, CTO, and STO are incipient ferroelectrics where either quantum fluctuations (STO) suppress the polar instability [2] or the mode energy remains too high to show finite temperature freezing (ETO, CTO). A pronounced analogy exists between STO and ETO [3,4], namely their cell parameters are almost identical and their dynamical behavior with respect to a transverse zone boundary instability follows the same temperature dependence [5,6]. What makes

ETO distinctly different from the other titanates is that its *A*-site ion Eu^{2+} is in the $4f^7$ configuration enabling magnetism, which is realized at very low temperature, as *G*-type antiferromagnetism with $T_N = 5.5$ K [7,8]. This property has invoked considerable new interest in ETO, since promising multiferroic properties can be anticipated [9]. Indeed, strained ETO films have been suggested to show polar properties [10,11], but ferroelectricity has only indirectly been attributed to this state. However, strain is a proper tool to change the antiferromagnetic properties to ferromagnetic ones as has been verified by magnetostriction experiments [12]. Another striking attribute of ETO is the hidden magnetism at high temperature which becomes apparent by shifting its structural phase transition temperature at $T_S = 282$ K to higher temperatures under the action of a magnetic field [13]. Further evidence for some kind of magnetic activity at high temperatures has also been obtained from zero-field muon spin rotation (μSR) experiments where finite magnetically correlated clusters have been detected [14]. These features have been explained within a spin-lattice coupled approach, where the interplay between the lattice dynamics and the $4f^7$ spins leads to an additional and lattice modified exchange interaction on the one hand and an enhancement of T_S as compared to STO on the other hand [15].

Recently we were able to fabricate high-quality transparent epitaxial thin films of ETO on an STO substrate and obtained (001)-oriented unstrained films where the antiferromagnetic transition at $T_N = 5.5$ K was well documented and the transition at T_S proven. This methodology was chosen to

*a.bussmann-holder@fkf.mpg.de

Published by the American Physical Society under the terms of the [Creative Commons Attribution 4.0 International](https://creativecommons.org/licenses/by/4.0/) license. Further distribution of this work must maintain attribution to the author(s) and the published article's title, journal citation, and DOI. Open access publication funded by the Max Planck Society.

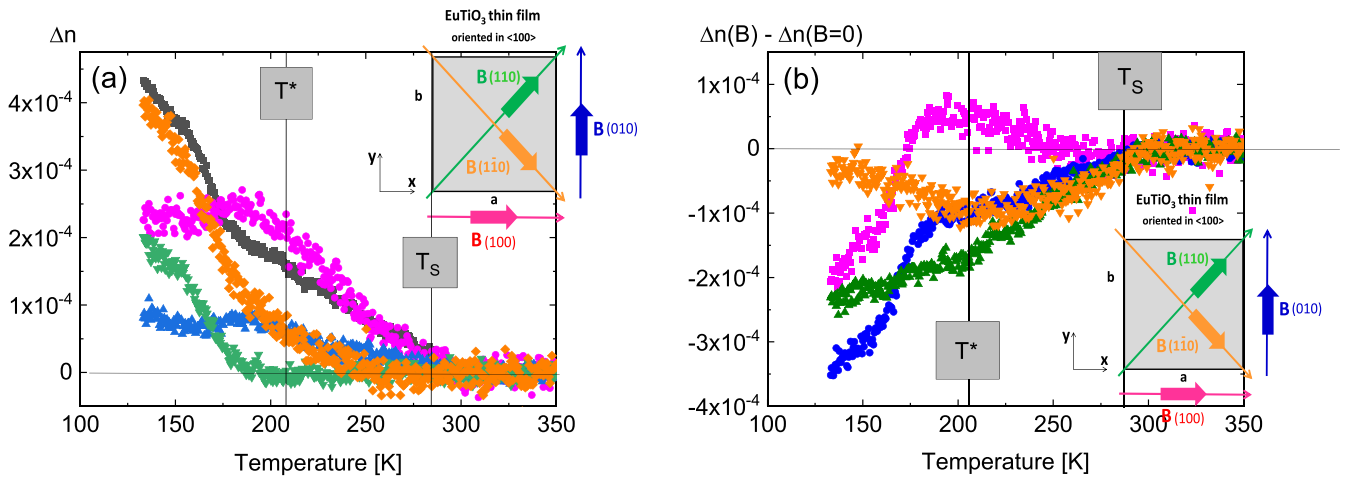


FIG. 1. (a) Birefringence Δn of ETO as a function of temperature. The black data points are obtained without magnetic field; the colored points are obtained in an external magnetic field $B = 0.02$ T with changing direction. Color code refers to the inset where the directions of the field are shown. (b) Birefringence difference $\Delta n(B) - \Delta n(B=0)$ as a function of temperature in an external directional magnetic field for the data shown in (a). Two transition temperatures T_S and T^* are marked by vertical lines.

demonstrate that the films exhibit bulk properties and interfacial effects are unimportant. In addition, any consequences of strain, which can have substantial effects on the ground-state properties, can be excluded. Furthermore, the small lattice mismatch between ETO and STO substrate promotes the limited interfacial strain. These films had considerable advantages as compared to previously obtained ceramic bulk samples, since they admitted to measure birefringence, an excellent tool to detect symmetry changes [16,17]. From these data T_S could clearly be documented and evidence for a further phase transition around 210 K was obtained as speculated previously. Under the action of a small magnetic field, substantial changes in the domain patterns and in the onset temperature were observed where a pronounced directional field dependence was seen [18]. From these experiments it was concluded that the symmetry of ETO below T_S had to be lower than tetragonal followed by an even lower-symmetry phase around $T^* \approx 210$ K. These findings were supported by μ SR and high-quality synchrotron XRD data, both detecting the lower-symmetry phase around 210 K and the possibility that the nominally tetragonal phase has lower symmetry [14,19,20].

II. BIREFRINGENCE RESULTS

In the following, the recent birefringence [18] and x-ray-diffraction (XRD) results [21] are complemented by systematic temperature-dependent birefringence Δn data in order to arrive at conclusions related to the symmetry lowering below T_S and possible magnetic anisotropies connected with it. In addition, results of the magnetic field dependence along high-symmetry directions are presented for various temperatures below T_S and compared to each other and to data obtained above T_S . The data on the films have been taken perpendicular to the c axis, i.e., refer to the EuO/TiO₂ planes. As outlined above, the film thickness was chosen intentionally to be very thick, i.e., 1000 nm, to make sure that all measurements test bulk properties. For details about the measurement technique, we refer to Refs. [16,18].

The birefringence of ETO was measured with the MetriPol Birefringence Imaging System (Oxford Cryosystems), which consists of a polarizing microscope equipped with a computer-controlled plane polarizer capable of being rotated to fixed angles α from a reference position, a circularly polarizing analyzer, and a charge-coupled device camera. In all experiments the wavelength of light of 570 nm was used. The outcome of the previously obtained birefringence Δn study [18] is summarized in Fig. 1(a) where the global Δn without an external field (black symbols) together with the results obtained under the influence of a directional magnetic field on Δn is depicted. By comparing the temperature dependence of Δn between the various magnetic field orientations and the field-free case we clearly see that the cubic to pseudotetragonal phase transition associated with T_S is strongly affected by the magnetic field orientation. For the (110) and (1-10) of the magnetic field direction a suppression of the (cubic) C- (pseudotetragonal) T structural phase transition is observed whereas for the magnetic field orientation along (100) and (010) directions a negligible effect is observed. These findings suggest that in ETO there is a strong interplay between the existence of this C-T phase transition and short-range magnetic interactions. This is in line with previous XRD [21] and Raman [22] results suggesting those magnetic interactions are the driving force of the C-T structural phase transition at 282 K. Obviously, there are distinct differences between the data taken in zero and nonzero magnetic field. Very striking is especially the temperature dependence below $T^* \approx 210$ K, where the field leads to an apparent splitting of the field-dependent results. In addition, the direction-dependent application of the magnetic field on Δn is for all field directions distinctly different, showing directly the inequality of the four axes investigated. This is incompatible with tetragonal symmetry. From both datasets, i.e., $B = 0$ and B finite, two temperature scales clearly emerge, namely the structural transition temperature T_S at 282 K and the previously discovered temperature T^* around 210 K. It is important to note that T_S is strongly influenced by the magnetic field along the diagonal directions (110) and (1-10). For

the two other directions Δn adopts finite values and increases with decreasing temperature, however, with different slopes highlighting again the disparity between these orthogonal directions. Below T^* the slope of all Δn curves changes and finite values along the diagonals signal a further symmetry lowering. The influence of the field on Δn is more clearly seen by plotting the difference $\Delta n(B) - \Delta n(B = 0)$ as is shown in Fig. 1(b). Along the (100) direction the magnetic field enhances the birefringence, whereas in the orthogonal and the two diagonal directions an almost identical reduction takes place, which changes abruptly at T^* . While along the main axis (100) and (010) Δn decreases with different slopes, it increases abruptly along (1-10), whereas a small decrease in the orthogonal direction takes place. From both figures it is, however, evident that below T_S and T^* neither the (100) direction is equivalent with (010), nor (110) with (1-10), demonstrating that at least in a magnetic field the crystal structure must be lower than tetragonal. This directional anisotropy allows additionally to also exclude orthorhombic symmetry where the diagonal orientation pictures should be identical. Also, all data strongly suggest the existence of another symmetry lowering below T^* in accordance with a number of earlier data [17]. An even more clear picture is provided by the difference optical orientation $\Delta\varphi$ maps [18] in Figs. 2(a)–2(e), where the $B = 0$ and B -finite directional data are compared to each other for specific temperatures below T_S and below the temperature scale $T^* < 210$ K. In order to clearly highlight the effect of the structural phase transition at T_S on Δn , also data taken well above T_S are shown [Fig. 2(f)] which yield the expected featureless picture characteristic of the high-symmetry cubic phase. For clarity, in the same figure the experimental setup of the sample in a magnetic field is shown.

All images of Figs. 2(a)–2(e) differ from the others and do not only show the effect of temperature on the domain structure, but also the effect of the magnetic field in the four directions. Starting with Fig. 2(a) ($B = 0$) the lowering of temperature (from right to left) influences the stripelike patterning. At 210 K the stripes become more brilliant and broader, possibly caused by the phase-change temperature at T^* , since at $T = 130$ K this effect is strongly increased. Distinctly different patterns appear under the influence of the magnetic field. With the field along the (1-10) direction [Fig. 2(b)] a checkerboard design develops which gets more pronounced around T^* and even further at 130 K. Upon turning the field by 180° [Fig. 2(c)] the checkerboard pattern has vanished, and stripy features develop which have almost disappeared around T^* and reappear more clearly at 130 K. Also, the color code has changed considerably, and only two different colors, i.e., two different indicatrix orientations, are observed. Note, in tetragonal symmetry both directions (110) and (1-10) should be equivalent. However, as can be seen in Figs. 2(b) and 2(c), there are considerable differences between these two directions which directly admits to excluding tetragonal symmetry. In addition, in orthorhombic symmetry also both directions are identical in their domain pattern, which further demonstrates that the symmetry must be even lower than orthorhombic. Figures 2(d) and 2(e) show the other orthogonal directions, namely (010) and (100), where stripelike domains develop along the field direction for the first case while contrasting featureless domains are

seen in the perpendicular one, which are hardly detectable at 130 K. In agreement with the above observations, it is obvious that these two directions are not equivalent. Most striking is, however, the magnetic field influence on Δn [18] which supports all earlier conclusions that some type of hidden magnetism is present in ETO. Especially, the data along (1-10) and (110) highlight this influence, wherein the latter stripes along the field direction form, suggesting magnetically influenced domains with spin interchanging character, while in the former the checkerboard pattern is seen which could stem from ordered spin-up and spin-down configurations and possibly some frustrated state. In both cases, the total spin would be zero and thus a bulk magnetic state would not be detectable. In Fig. 2(f) the same data as above are shown at 300 K, i.e., well above T_S , where the left figure refers to the orientational map whereas the middle is the difference picture between temperatures ($T = 320$ K – $T = 300$ K). As expected, in cubic symmetry no domains are seen, and a homogeneous state is observed. Summarizing the above results two conclusions emerge, namely the disparity between the two orthogonal directions is incompatible with tetragonal and orthorhombic symmetry suggesting that a lower symmetry must be realized, and an external magnetic field induces substantial changes in the domain configuration which demonstrates magnetic activity far above T_N . For the above reasoning, also rhombohedral symmetry is incompatible with the observations.

Since the Metripol technique measures the orientation angle φ [see Fig. 2(a) for its definition], presented as a colored map (see Figs. 2) in which different colors are related to different angles φ , it enables the visualization of the distribution of these orientations. The distribution of orientations δ_d (histogram), i.e., the number of domains (expressed as a percentage of all domains) with the optical axis oriented under φ to the x axis, can be calculated based on such maps. Each point of such a histogram corresponds to the orientation distribution calculated for a 1° interval. This analysis has been done for the data shown in Fig. 2(a) collected with no B field and for the data in Fig. 2(b) detected for $B = 0.2$ T directed along the (1-10) direction. Histograms for temperatures $T < T_S$ and $T < T^*$ and $B = 0$ are shown in Figs. 3. The data have been fitted with two Gauss functions and a constant background, which accounts for the noise of the randomness in domain distribution.

Apparently, a maximum in δ_d occurs around $\approx 75^\circ$ (blue arrow) and a rather broad and not well-resolved one near 23° (green arrow). Both these angles are incompatible with symmetries related to tetragonal, orthorhombic, or rhombohedral, but well explainable in monoclinic M_A , M_B structures, since they do not occur at high-symmetry angles 45° , 90° , 135° , and 180° expected for the above-mentioned symmetries. While for $T_S > T = 260$ K $> T^*$ the lower angle peak is rather flat, this grows considerably in intensity for $T^* > T = 170$ K together with the other one. A shift in the peaks' positions is hardly visible and if so, hidden by the broad features and the background. The same data have been obtained for a finite, small, magnetic field of $B = 0.1$ T which are displayed in Figs. 4 for the same temperatures as in Figs. 3.

The magnetic field has the effect that in the temperature range $T_S < T < T^*$ the blue peak moves to smaller angles whereas the green one diminished in intensity. This suggests,

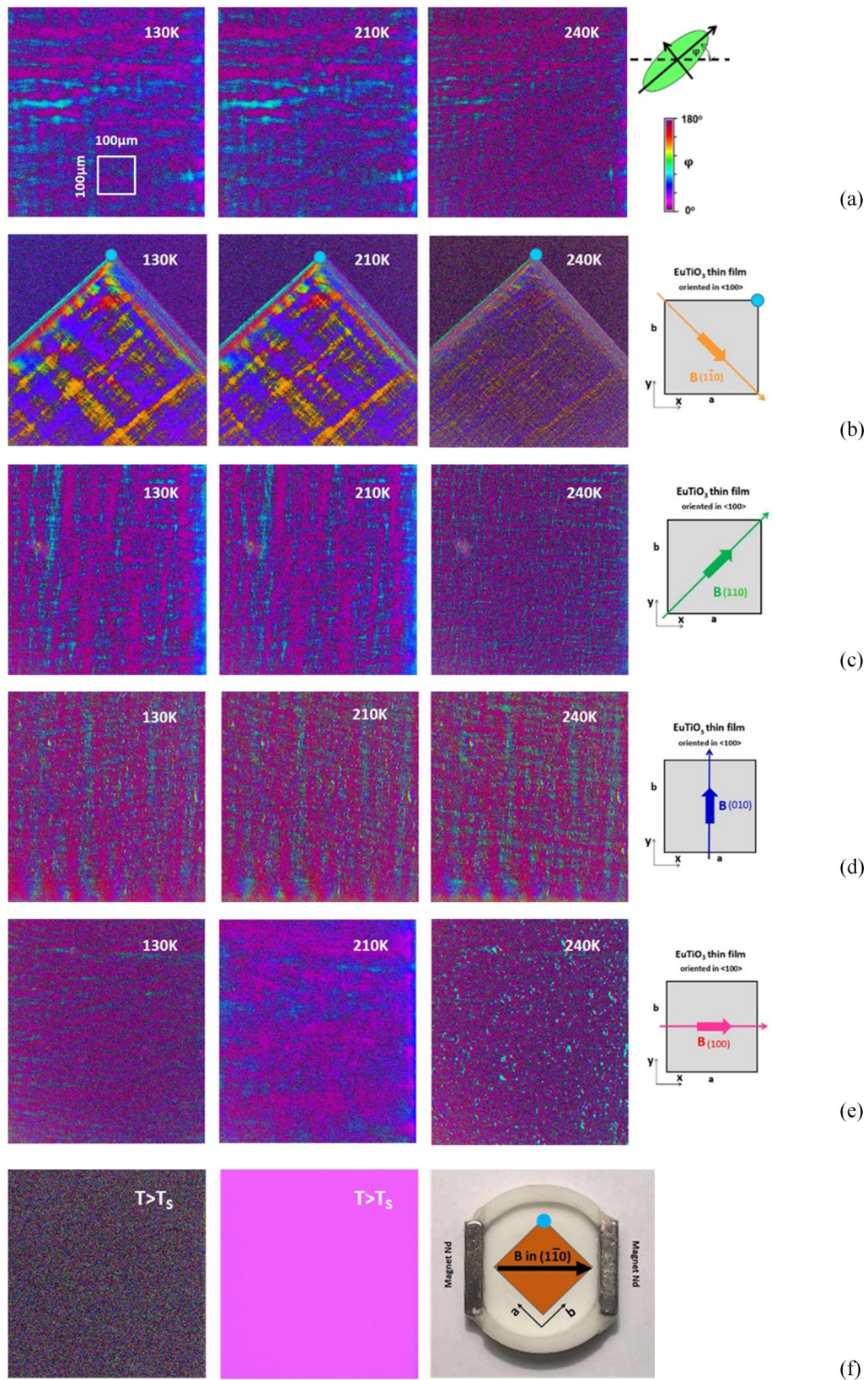


FIG. 2. Difference orientation maps of thin-film ETO samples at temperatures of 130 K (left), 210 K (middle), and 240 K (right). (a) refers to $B = 0$; in (b)–(e) $B = 0.02$ T. Magnetic field directions are as given in the small squares to the right of the respective figure. Next to (a) a color code for the indicatrix is shown. All the images were taken on the same area of the same sample, and the scale in (a) is the same for all images. Images in b) are rotated by 45° , because of the sample holder construction in which the thin film was placed, as shown in (f) on the right. The sample holder contains two fixed Nd magnets producing the magnetic induction B . Thin film was rotated inside the holder to get a defined orientation to the magnetic field. (f) Orientational (spotty black) picture and the difference (320 K–300 K) birefringence map (pink) with $B = 0$ above T_S show the ETO film’s homogeneous structure (no difference in map color intensity) on the STO substrate.

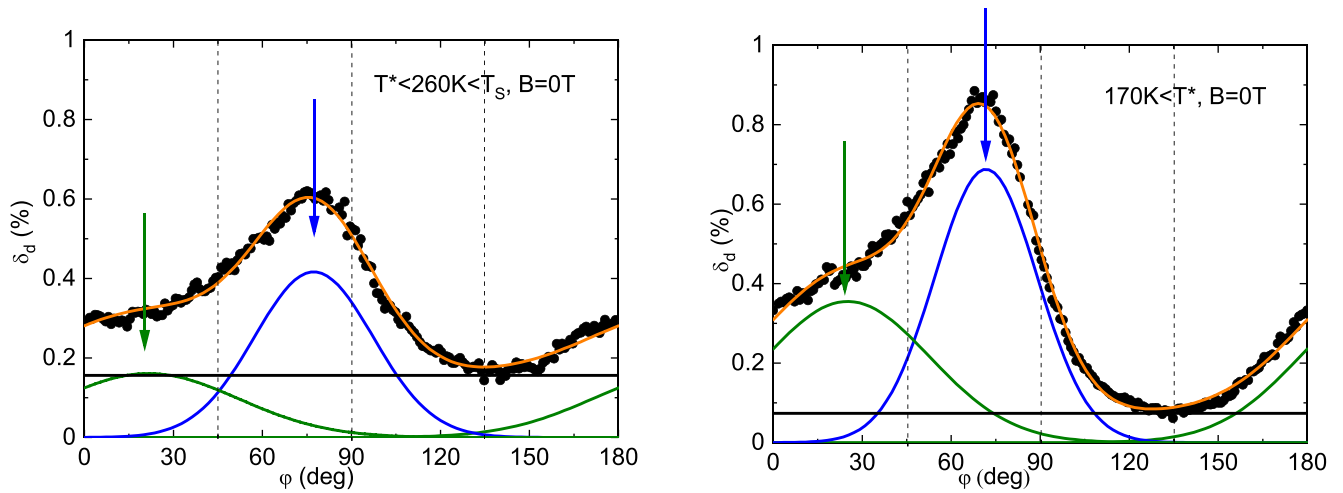


FIG. 3. Distribution of orientations δ_d as a function of the optical axis orientation φ for $T = 260$ K (left) and 170 K (right) in the absence of a magnetic field (black filled circles). The blue and green arrows at 260 and 170 K indicate the maxima of the fitted Gaussian distributions of φ , corresponding to monoclinic symmetries. The orange curve is cumulative, and the green curve represents the background originating, among others, from overlapping domains of different thicknesses, numerous domain boundaries, and possibly the STO substrate on which the ETO thin film was deposited. The straight black line is the background. Note that while at 260 K this is finite, it is almost zero at 170 K. We attribute this to the fact that far below T_S and well below T^* the domain formation is more robust, which is also evident from the green and blue peaks narrowing and their increase in strength. Dashed black vertical lines correspond to the high-symmetry angles $\varphi = 45^\circ$, 90° , and 135° .

as already speculated from the XRD data [22] that the field tries to restore the pseudotetragonal phase. However, below T^* the shift is absent and both the green and blue peaks gain weight. This latter observation is attributed to magnetic frustrations, which become dominant. A detailed understanding

is missing, and it is suggested to study the transitions in the presence of larger fields, which is presently impossible in our experimental setup. As in the previous case, distinguishing between monoclinic phases M_A and M_B needs advanced structural investigations.

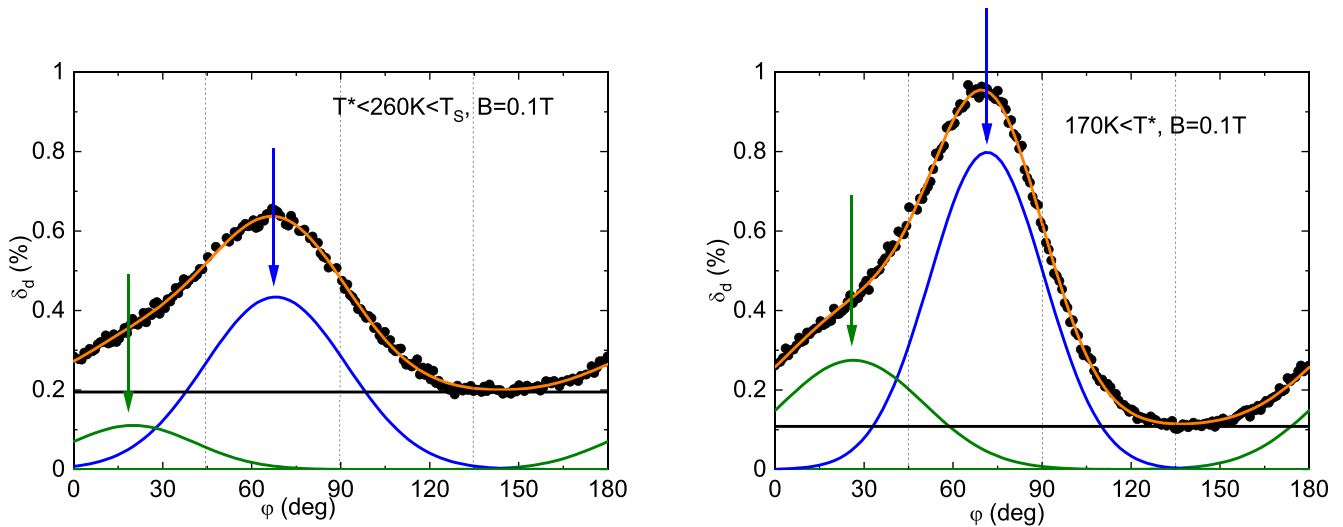


FIG. 4. Distribution of orientations δ_d (black filled circles) as a function of the optical axis orientation φ for $T = 260$ K (left) and 170 K (right) in a magnetic field $B = 0.1$ T. Blue and green arrows highlight the maxima expected in monoclinic symmetry. As in Figs. 3, the straight black line represents the constant background originating, among others, from overlapping domains of different thicknesses, numerous domain boundaries, and the STO substrate on which the ETO thin film was deposited. It is related to the theoretical consideration that the transition from the cubic to the monoclinic phase creates 12 ferroelastic domain variants. These can pair with each other along 84 types of domain walls as applicable to the monoclinic phases of M_A , M_B , and M_C types, discussed further in the text [23–25]. With such a large number of domains and domain walls, the existence of the background, and its changes under the magnetic field action, is comprehensible. This background is different from that in Fig. 3 and much stronger, which we assume to stem from the diagonal orientation of the magnetic field which, as is visible in Fig. 2(b), strongly affects the domain formation. The dashed black vertical lines correspond to the high-symmetry angles $\varphi = 45^\circ$, 90° , and 135° .

III. XRD RESULTS

In order to find out what is magnetically happening, the recently published high-quality synchrotron XRD data [22,26] have been analyzed in deeper detail and XRD data at grazing incidence from the film are presented. The previously reported EuO refined distances EuO1, EuO2A, and EuO2B, referring to, respectively, the EuO apical, the planar short and long EuO distances [see Fig. 5(a)] for their definition) have been taken as input to derive the corresponding “pseudocubic” unit-cell parameters. These have been normalized [22] to the value at $T = 300$ K, i.e., $a_0 = 3.905$ Å (Fig. 5). With this approach we can plot the equivalent pseudocubic lattice properties as a function of temperature that depends on a given Eu-O distance. We choose this approach, since the J_1 , J_2 exchange parameters [for their definition see Fig. 5(a)] have been calculated from the pseudocubic lattice constant, thus, our experimental values can be easily used as inputs to our phenomenological model.

In addition, signatures of a further phase transition around T^* [27] have been reported which are visible in Figs. 5(b)–5(f), where straight lines in (b)–(e) show linear in temperature regimes with a clear break in slope around 210 K. While the data in Figs. 4(b) and 4(d) have been obtained in a small magnetic field of $B = 480$ mT, those displayed in Figs. 5(c) and 5(e) refer to $B = 0$ T. In Figs. 5(d) and 5(e) the half of the average distance of the in-plane EuO bonds is compared to the apical one, which provides a signature of the planar oxygen displacements and is also associated with the oxygen octahedral rotation. This latter statement is based on the fact that in Figs. 5(d) and 5(e) normalized pseudocubic lattice constants have been plotted. In strictly cubic symmetry, where no oxygen distortions are present, half of the sum of the in-plane normalized lattice constants is identical to the normalized c-axis lattice constant as depicted in Figs. 5(b) and 5(c). However, in the enlarged Figs. 5(d) and 5(e) it is clear that distinct differences exist, which signify the presence of a distortion of the oxygen sites associated with a symmetry lowering. Note, that these lattice constants have been derived from the refined three EuO distances and normalized to a pseudocubic lattice. Very striking is the magnetic field effect [Figs. 5(b) and 5(d)] on the lattice. Apparently, the field appears to reduce the pseudotetragonal distortion and the octahedral rotation, whereas the temperature T^* effect becomes more pronounced. The size of this effect is comparable to the one observed upon the onset of antiferromagnetic (AFM) order at the Néel temperature T_N , where magnetostriction leads to a spontaneous shrinking of the lattice constant. This might imply that the magnetic field supports local AFM ordering; however, further investigations are needed to provide a plausible explanation. The ETO film has additionally been characterized at $B = 0$ mT in the temperature range 100–300 K with synchrotron grazing-incidence x-ray diffraction (GIXD) at the XRD1 beamline of Elettra Sinchrotrone, Trieste. Integrated images have been recorded on a 2D Pilatus 2M detector (with $\lambda = 0.7$ Å) while continuously rotating the crystal about the surface normal keeping constant the incidence angle α_i . Indexing and analysis of the observed diffraction peaks have been performed after reshaping the GIXD images to reciprocal-space axes using the GIDVIS software and a LaB₆ standard for calibration of the

detector distance [28]. All diffraction images show a highly textured structure as expected from an epitaxial film and could be successfully indexed as cubic at 300 K. Twelve reflections have been used to refine the corresponding unit-cell parameters of the average “cubic” lattice in the temperature range 100–300 K using the program UNITCELL [29]. In Fig. 5(d) the equivalent cubic lattice constant is plotted as a function of temperature without an external magnetic field. In Fig. 5(f) the data from two incidence angles at nominal values 0° and 1° are presented to uncover lattice modifications at the very surface of the 1- μm film in comparison with the rest of it. Even with the 1° incidence angle only the film is probed and any contribution from the homologous SrTiO₃ substrate is negligible; thus, any interfacial effects and artifacts can be completely excluded, since we observe qualitatively the same behavior in the whole depth of the film. Obviously, a sharp drop in the lattice constant takes place at T^* which becomes more pronounced when measuring at large α_i . This observation is thus a clear manifestation of a second structural phase transition at T^* which has not been detected so clearly before.

IV. THEORY

In the following, these data are taken as input to arrive at conclusions about the kind of magnetism at high temperatures and the possible symmetries below T_S and T^* . For this reason, the nearest- and next-nearest neighbor exchange interactions J_1 , J_2 of ETO [they are defined as indicated in Fig. 5(a)] are derived, since their distance dependence is known from the pressure dependence of T_N [27–29]. By extracting from the measured EuO distances, EuO2A, EuO2B, and EuO1 [see Fig. 5(a)] the corresponding effective cubic unit-cell parameters a , these two quantities are obtained for each EuO distance according to [30]

$$J_1 = J_1^0 \left(\frac{a}{a_0} \right)^{-20.9}, \quad J_2 = J_2^0 \left(\frac{a}{a_0} \right)^{-10.8}, \quad (1)$$

where $\frac{J_1^0}{k_B} = -0.015$ K, $\frac{J_2^0}{k_B} = +0.036$ K are the exchange interactions for the ideal case, and a_0 is the lattice constant measured at 300 K. a is the unit-cell parameter evaluated from the measured EuO distances for the ideal case that the lattice is cubic. The thus-obtained exchange constants [Fig. 6(a)] are further used to calculate T_N :

$$T_N = \frac{2S(S+1)}{3k_B} (-6J_1 + 12J_2). \quad (2)$$

While the results for large and small unit-cell parameters show an almost linear dependence of J_1 , J_2 on a [Fig. 6(a)], an intermediate regime appears for a as derived from the apical distance with a clear break with respect to the limiting regions. In this small regime J_1 , J_2 are closest to J_1^0 , J_2^0 . The more a is increasing, decreasing, both quantities decrease, increase systematically reflecting the tendency to revert to ferro-, respectively, increased antiferromagnetic, properties. Note that Eqs. (1) and (2) refer to the low-temperature regime ($T < T_N$) and might thus be meaningless in the considered region, however, and as has been shown in Refs. [12,31], tiny

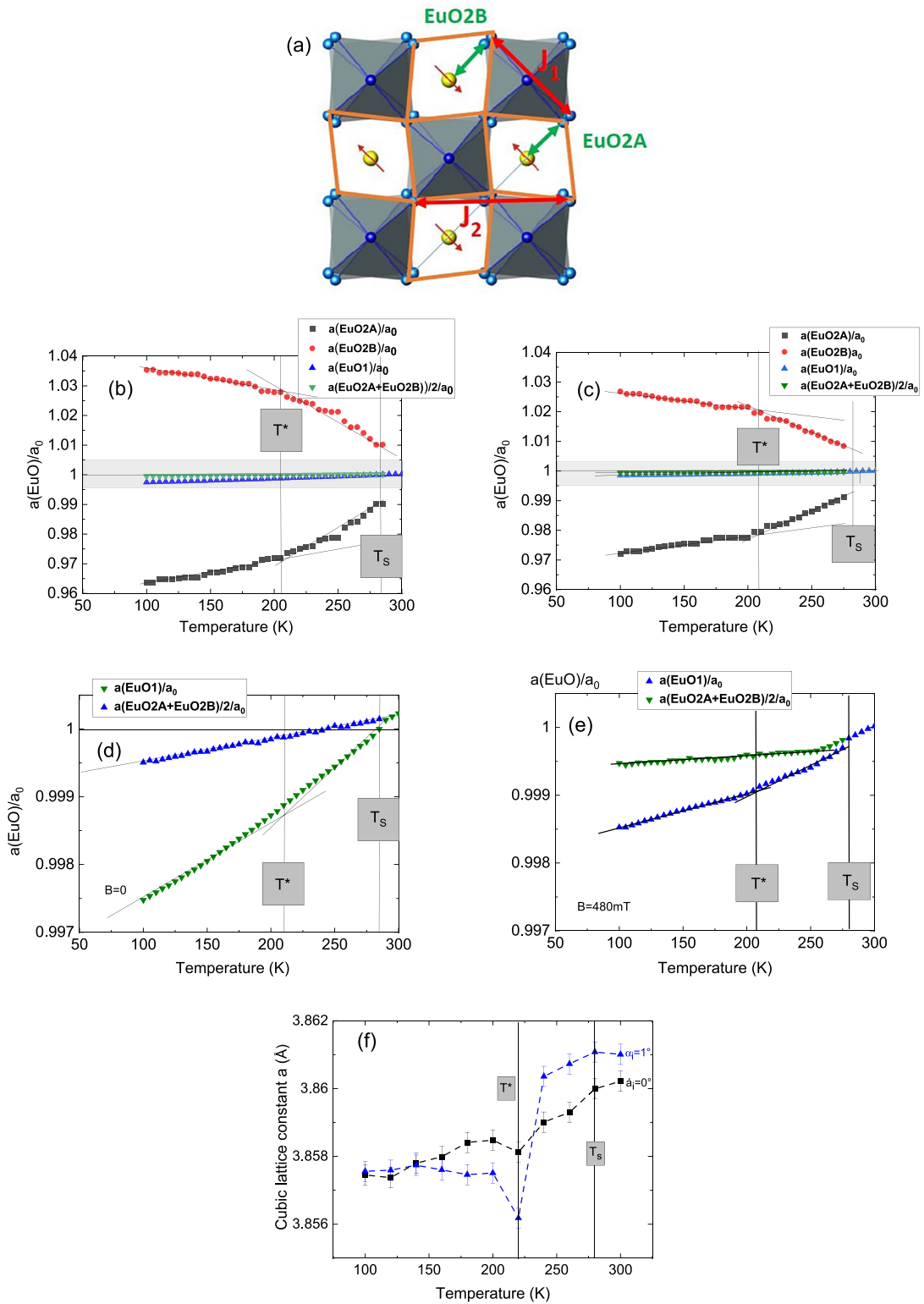


FIG. 5. (a) c -axis projected lattice of ETO where the nearest- and next-nearest neighbor exchange interactions J_1 , J_2 are indicated together with the planar EuO distances $2A$ and $2B$. Since the figure is a projection on the planes, the EuO distance along the c -axis is not shown here. (b) Temperature dependence of the normalized unit-cell parameters for the three EuO bond distances as extracted from XRD data in zero magnetic field and (c) in a field of 480 mT. (d) shows an enlarged part of the main figure [light gray shaded area in (b), (c)] where half the average of EuO2A and EuO2B is shown and compared to EuO1 with magnetic field $B = 0$ T, and (e) $B = 480$ mT. In cubic symmetry without oxygen octahedral rotation, these should be identical. (f) Corresponding pseudocubic unit-cell parameters as a function of temperature at two grazing-incidence angles $\alpha_i = 0^\circ$, 1° where the increasing $\alpha_i = 1^\circ$ marks the deeper bulk testing measurement (dashed lines are a guide to the eye, error bars in (d) represent estimated standard deviation of refined values, and vertical lines indicate T^* , T_S). In all datasets, T^* is well visible whereas T_S is less well marked.

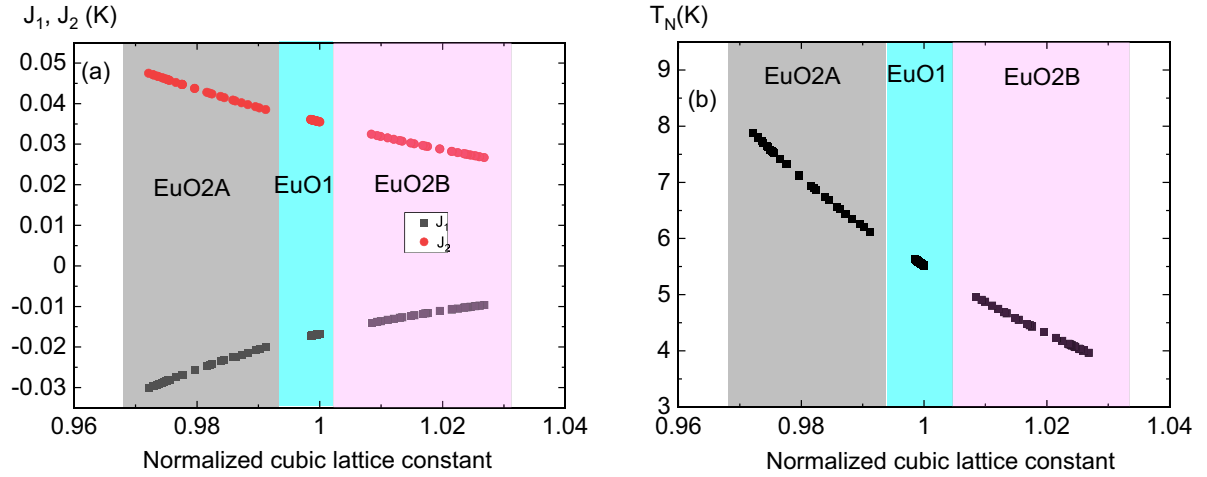


FIG. 6. (a) J_1, J_2 as functions of the EuO bond distances. Black points refer to J_1 , red to J_2 . The shaded areas indicate the regions where EuO2A (gray), EuO1 (light turquoise), and EuO2B (light pink) lie. EuO1 seems to correspond to some “equilibrium” distance. (b) Néel temperature T_N as derived from the exchange interactions as given in (a) with the same color code as above. While the known increase in T_N with decreasing unit-cell parameter is followed overall, the EuO1 related data points mark a crossover from the limiting linear regimes appearing for larger and smaller lattice constants.

changes in the lattice constant as observed here have huge effects on the magnetic ordering.

With the knowledge of J_1, J_2 , [Fig. 6(a)] the bond-dependent Néel temperature [Fig. 6(b)] is determined with the assumption of a cubic lattice and the lattice constant as described above [Eq. (2)]. As was expected from the exchange constants T_N almost linearly increases with decreasing distance and exceeds the ambient value by more than 50% for the smallest EuO distances. With increasing distances T_N rapidly moves almost linearly to lower values in accordance with the fact that strained ETO [10] changes from antiferro- to ferromagnetic order. For small and large distances the dependence of T_N on these is almost linear, whereas the intermediate c -axis related ones mark a crossover between the two regions.

From earlier work it is known that three magnetic ground states are energetically close together [5,30]. These are the ferromagnetic case (FM), the antiferromagnetic case 1 (AFM1) where the interlayers are antiferromagnetically arranged, and the antiferromagnetic case 2 where each Eu site is antiferromagnetically surrounded by its neighbors (AFM2), i.e., G type.

The energies of these states per formula unit (FU) are given by [32]:

$$\begin{aligned} E_{FM} &= (-3J_1 - 6J_2) \left(\frac{N^2}{4} \right), \\ E_{AFM1} &= (-J_1 + 2J_2) \left(\frac{N^2}{4} \right), \\ E_{AFM2} &= (+3J_1 - 6J_2) \left(\frac{N^2}{4} \right). \end{aligned} \quad (3)$$

These are energy expressions for spin dimers with N unpaired spins per site, where $N = 7$ in the present case.

The results for the exchange interactions, the Néel temperature, and the above energies are shown in Figs. 6(a) and 6(b), and Fig. 7 using the above assumptions.

As is obvious from Fig. 7, the G -type antiferromagnetic order (AFM2) has always the lowest energy whereas the AFM1 state can be excluded from further considerations. Very close to it lies the FM state which gets more and more stable with decreasing unit-cell parameter and competes with AFM2 if the distances EuO2A and EuO2B differ by $\approx 0.15 \text{ \AA}$ [see Fig. 5(a)]. However, if one considers three coexisting distances as observed experimentally and realized by oxygen octahedral rotations, the situation can become increasingly complex even if AFM2 remains the lowest-energy state. Experimentally, it is known that even small lattice dilatations induce ferromagnetism [12], much smaller than obtained on

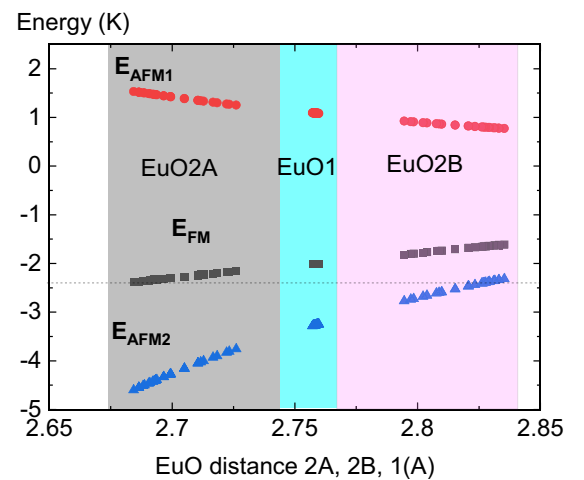


FIG. 7. Above-defined energies E_{FM}, E_{AFM1} , and E_{AFM2} [Eq. (3)] as a function of the EuO bond distances with the same color code as used in Fig. 6. For the smallest distances the lowest-energy states with AFM2 order are obtained with raising energy for larger distances. Interestingly, the FM state related to EuO2A [see Fig. 5(a)] is close in energy to the AFM2 one for the longer bond (dashed line). This could lead to a frustration of the magnetic order.

the basis of the above theoretical concept, which suggests that for the longer planar EuO₂B bond FM order can become favorable, whereas for EuO₂A and EuO₁ AFM₂ is preferential. This scenario is clearly incompatible with any long-range magnetic order and supports frustration. In the presence of a small magnetic field, spin alignment also along the shorter EuO₂A bond can be expected, since the field expands the lattice and supports tetragonality in agreement with former and earlier observations [16,18]. Note that density-functional calculations (DFT) have been performed for ETO [33–36], which primarily concentrated on the crystal symmetry below T_N [33,34]. In accordance with the above analysis the general conclusion was that all considered space groups are extremely close in energy (differing by some meV only), thereby disabling conclusions on the true symmetry of the low-temperature structure. After the discovery of the nominally cubic tetragonal phase transition (based on lattice dynamical predictions) more detailed DFT studies have been carried through all, confirming the $I4/mcm$ structure to be the correct one.

V. CONCLUSIONS

In view of the above results, it cannot be expected that the “hidden” magnetism is uniform throughout the sample but that different magnetic states must coexist in some kind of domains/clusters, which on the average cancel out any macroscopic magnetic moment. The external field supports locally spin-aligned structures and creates new ones [see Fig. 2(b)], but cannot drive the system into a homogeneous

magnetically ordered state. This is also in agreement with our observation that two monoclinic phases coexist for $T < T_S$. We conclude that ETO represents an extremely complex perovskite where the lattice and the spins are intimately coupled, thereby causing textures in the spin arrangement and the crystal symmetry. Our data are incompatible with tetragonal, orthorhombic, or rhombohedral symmetry below T_S or T^* , but can only be explained by monoclinic C_m (M_A , M_B) symmetry with polar properties. In summary, we have clearly proven that ETO represents the only perovskite oxide which does not follow the classical phase transition sequence observed in all other oxide perovskites, namely, cubic→tetragonal→orthorhombic→rhombohedral, but instead cubic→monoclinic.

All data generated or analyzed during this study are included in this article including the references.

ACKNOWLEDGMENTS

P.P. and E.L. acknowledge support by the project CALIP-SOplus under Grant Agreement No. 730872 from the EU Framework Programme for Research and Innovation HORIZON 2020 for the synchrotron XRD data obtained at Elettra Sincrotrone. P.P. and E.L. would like to thank M. Calamiotou for helpful remarks and the XRD1 staff L. Barba.

A.B.-H. initiated the project and contributed with theoretical considerations; E.L. and P.P. performed the XRD experiments; and K.R. carried out the birefringence experiments. H.K. contributed with important discussions and in writing the manuscript.

-
- [1] A. Bussmann-Holder, K. Roleder, and J.-H. Ko, What makes the difference in perovskite oxides, *J. Phys. Chem. Solids* **117**, 148 (2018).
 - [2] K. A. Müller and H. Burkard, SrTiO₃: An intrinsic quantum paraelectric below 4 K, *Phys. Rev. B* **19**, 3593 (1979).
 - [3] S. Kamba, D. Nuzhnyy, P. Vaněk, M. Savinov, K. Knížek, Z. Shen, E. Šantavá, K. Maca, M. Sadowski, and J. Petzelt, Magnetodielectric effect and optic soft mode behavior in quantum paraelectric EuTiO₃ ceramics, *Europhys. Lett.* **80**, 27002 (2007).
 - [4] V. Goian, S. Kamba, J. Hlinka, P. Vaněk, A. A. Belik, T. Kolodiaznyi, and J. Petzelt, Polar phonon mixing in magnetoelectric EuTiO₃, *Eur. Phys. J. B* **71**, 429 (2009).
 - [5] J. L. Bettis, M.-H. Whangbo, J. Köhler, A. Bussmann-Holder, and A. R. Bishop, Lattice dynamical analogies and differences between SrTiO₃ and EuTiO₃ revealed by phonon-dispersion relations and double-well potentials, *Phys. Rev. B* **84**, 184114 (2011).
 - [6] D. S. Ellis, H. Uchiyama, S. Tsutsui, K. Sugimoto, K. Kato, D. Ishikawa, and A. Q. R. Baron, Phonon softening and dispersion in EuTiO₃, *Phys. Rev. B* **86**, 220301(R) (2012).
 - [7] J. Brous, I. Frankuchen, and E. Banks, Rare earth titanates with a perovskite structure, *Acta Crystallogr.* **6**, 67 (1953).
 - [8] T. R. McGuire, M. W. Shafer, R. J. Joenk, H. A. Halperin, and S. Pickart, Magnetic structure of EuTiO₃, *J. Appl. Phys.* **37**, 981 (1966).
 - [9] T. Katsufuji and H. Takagi, Coupling between magnetism and dielectric properties in quantum paraelectric EuTiO₃, *Phys. Rev. B* **64**, 054415 (2001).
 - [10] J. H. Lee, L. Fang, E. Vlahos, X. Ke, Y. W. Jung, L. F. Kourkoutis, J.-W. Kim, P. J. Ryan, T. Heeg, M. Roeckerath *et al.*, A strong ferroelectric ferromagnet created by means of spin–lattice coupling, *Nature* **466**, 954 (2010).
 - [11] P. Pappas, M. Calamiotou, J. Köhler, A. Bussmann-Holder, and E. Liarakis, Nonlinear electrostrictive lattice response of EuTiO₃, *Appl. Phys. Lett.* **111**, 052902 (2017).
 - [12] P. G. Reuvekamp, R. K. Kremer, J. Köhler, and A. Bussmann-Holder, Spin-lattice coupling induced crossover from negative to positive magnetostriction in EuTiO₃, *Phys. Rev. B* **90**, 094420 (2014).
 - [13] Z. Guguchia, H. Keller, J. Köhler, and A. Bussmann-Holder, Magnetic field enhanced structural instability in EuTiO₃, *J. Phys.: Condens. Matter* **24**, 492201 (2012).
 - [14] Z. Guguchia, Z. Salman, H. Keller, K. Roleder, J. Köhler, and A. Bussmann-Holder, Complexity in the structural and magnetic properties of almost multiferroic EuTiO₃, *Phys. Rev. B* **94**, 220406(R) (2016).
 - [15] A. Bussmann-Holder, J. Köhler, R. K. Kremer, and J. M. Law, Relation between structural instabilities in EuTiO₃ and SrTiO₃, *Phys. Rev. B* **83**, 212102 (2011).

- [16] A. Bussmann-Holder, K. Roleder, B. Stuhlhofer, G. Logvenov, I. Lazar, A. Soszyński, J. Koerski, A. Simon, and J. Köhler, Transparent EuTiO₃ films: A possible two-dimensional magneto-optical device, *Sci. Rep.* **7**, 40621 (2017).
- [17] B. Stuhlhofer, G. Logvenov, M. Górný, K. Roleder, A. Boris, D. Pröpper, R. K. Kremer, J. Köhler, and A. Bussmann-Holder, New features from transparent thin films of EuTiO₃, *Phase Trans.* **89**, 731 (2016).
- [18] A. Bussmann-Holder, E. Liarokapis, and K. Roleder, Intriguing spin-lattice interactions in EuTiO₃, *Sci. Rep.* **11**, 18978 (2021).
- [19] G. Gregori, J. Köhler, J. F. Scott, and A. Bussmann-Holder, Hidden magnetism in the paramagnetic phase of EuTiO₃, *J. Phys.: Condens. Matter* **27**, 496003 (2015).
- [20] A. Bussmann-Holder, J. Köhler, K. Roleder, Z. Guguchia, and H. Keller, Unexpected magnetism at high temperature and novel magneto-dielectric-elastic coupling in EuTiO₃: A critical review, *Thin. Solid. Films* **643**, 3 (2017).
- [21] A. A. Bokov, X. Long, and Z.-G. Ye, Optically isotropic and monoclinic ferroelectric phases in Pb(Zr_{1-x}Ti_x)O₃ (PZT) single crystals near morphotropic phase boundary, *Phys. Rev. B* **81**, 172103 (2010).
- [22] P. Pappas, M. Calamiotou, M. Polentarutti, G. Bais, A. Bussmann-Holder, and E. Liarokapis, Magnetic field driven novel phase transitions in EuTiO₃, *J. Phys.: Condens. Matter* **34**, 02LT01 (2021).
- [23] S. Gorfman (private communication).
- [24] A. M. Glazer, J. G. Lewis, and W. Kaminsky, An automatic optical imaging system for birefringent media, *Proc. R. Soc. A: Math., Phys., Eng. Sci.* **452**, 2751 (1996).
- [25] S. Gorfman, A. M. Glazer, Y. Noguchi, M. Miyayama, H. Luo, and P. A. Thomas, Observation of a low-symmetry phase in Na_{0.5}Bi_{0.5}TiO₃ crystals by optical birefringence microscopy, *J. Appl. Crystallogr.* **45**, 444 (2012).
- [26] P. Pappas, E. Liarokapis, M. Calamiotou, and A. Bussmann-Holder, Magnetic interactions and the puzzling absence of any Raman mode in EuTiO₃, *J. Raman Spectrosc.* **52**, 914 (2021).
- [27] D. Bessas, K. Glazyrin, D. S. Ellis, I. Kantor, D. G. Merkel, V. Cerantola, S. van Smaalen Potapkin, Q. R. Baron, and R. P. Hermann, Pressure mediated structural transitions in bulk EuTiO₃, *Phys. Rev. B* **98**, 054105 (2018).
- [28] B. Schrode, S. Pachmaier, M. Dohr, C. Röthel, J. Domke, T. Fritz, R. Resela, and O. Werzer, GIDVis: A comprehensive software tool for geometry-independent grazing-incidence X-ray diffraction data analysis and pole-figure calculations, *J. Appl. Crystallogr.* **52**, 683 (2019).
- [29] T. J. B. Holland and S. A. T. Redfern, Unit cell refinement from powder diffraction data: The use of regression diagnostics, *Mineral. Mag.* **61**, 65 (1997).
- [30] Z. Guguchia, K. Caslin, R. K. Kremer, H. Keller, A. Shengelaya, A. Maisuradze, J. L. Bettis, Jr., J. Köhler, A. Bussmann-Holder, and M.-H. Whangbo, Nonlinear pressure dependence of T_N in almost multiferroic EuTiO₃, *J. Phys.: Condens. Matter* **25**, 376002 (2013).
- [31] M.-H. Whangbo, H.-J. Koo, and D. Dai, Spin exchange interactions and magnetic structures of extended magnetic solids with localized spins: Theoretical descriptions on formal, quantitative and qualitative levels, *J. Solid State Chem.* **176**, 417 (2003).
- [32] P. Reuvekamp, K. Caslin, Z. Guguchia, H. Keller, R. K. Kremer, A. Simon, J. Köhler, and A. Bussmann-Holder, Tiny cause with huge impact: Polar instability through strong magneto-electric-elastic coupling in bulk EuTiO₃, *J. Phys.: Condens. Matter* **27**, 262201 (2015).
- [33] H. Akamatsu, Y. Kumagai, F. Oba, K. Fujita, H. Murakami, K. Tanaka, and I. Tanaka, Antiferromagnetic superexchange via 3d states of titanium in EuTiO₃ as seen from hybrid Hartree-Fock density functional calculations, *Phys. Rev. B* **83**, 214421 (2011).
- [34] R. Ranjan, H. S. Nabi, and R. Pentcheva, Electronic structure and magnetism of EuTiO₃: A first-principles study, *J. Phys.: Condens. Matter* **19**, 406217 (2007).
- [35] R. Zhao, C. Yang, H. Wang, K. Jiang, H. Wu, S. Shen, L. Wang, Y. Sun, K. Jin, J. Gao, L. Chen, H. Wang, J. L. MacManus-Driscoll, P. A. van Aken, J. Hong, W. Li, and H. Yang, Emergent multiferroism with magnetodielectric coupling in EuTiO₃ created by a negative pressure control of strong spin-phonon coupling, *Nat. Commun.* **13**, 2364 (2022).
- [36] C. Li, J. Zhao, Z. Dong, C. Zhong, Y. Huang, Y. Min, M. Wang, and P. Zhou, Strain induced magnetic transitions and spin reorientations in quantum paraelectric EuTiO₃ material, *J. Magn. Magn. Mater.* **382**, 193 (2015).